Crystal growth / Croissance cristalline

Synchrotron X-ray imaging for crystal growth studies

Imagerie au rayonnement synchrotron pour les études de croissance cristalline

José Baruchel [a], Marco Di Michiel [a], Tamzin Lafford [a,*], Pierre Lhuissier [e],
Jacques Meyssonnier [d], Henri Nguyen-Thi [b,c], Armelle Philip [d], Petra Pernot [a], Luc Salvo [e],
Mario Scheel [a]

[a] ESRF, 6, rue Jules-Horowitz, BP 220, 38043 Grenoble, France
[b] Aix Marseille University, 13397 Marseille cedex 20, France
[c] CNRS, IM2NP, UMR CNRS 7334, campus Saint-Jérôme, case 142, 13397 Marseille cedex 20, France
[d] LGGE, UJF & CNRS, UMR 5183, 54, rue Molière, 38402 Saint-Martin-d'Hères, France
[e] Grenoble University & CNRS, SIMaP/GPM2, UMR CNRS 5266, UJF, BP 46, 38402 Saint-Martin-d'Hères, France

ARTICLE INFO

ABSTRACT

The features associated with modern synchrotron radiation machines (intense and coherent beams) result in a substantial extension of X-ray imaging capabilities in terms of spatial and temporal resolution, phase contrast and 3D images. This allows crystal growth-related information to be obtained which is not available otherwise. After briefly describing the main synchrotron radiation based imaging techniques of interest, we give original examples illustrating the new capabilities for crystal growth: characterisation of crystals grown for applications, such as ice tri-crystals produced for mechanical deformation studies; SiC; crystalline silicon for solar photovoltaic cells; in situ and in real time studies of quasicrystal growth (AlPdMn); and ultrafast tomography for the study of the growth of dendrites in metallic alloys.

© 2012 Académie des sciences. Published by Elsevier Masson SAS. All rights reserved.

RÉSUMÉ

Les caractéristiques des installations modernes de rayonnement synchrotron (faisceaux de rayons X intenses et cohérents) ont amené à une augmentation notable des possibilités des techniques d'imagerie, tant en ce qui concerne la résolution spatiale et temporelle que le contraste de phase et les images tridimensionelles. Ceci permet d'obtenir des informations sur la croissance cristalline qui ne peuvent être obtenues autrement. Après une brève description de techniques d'imagerie aux rayons X au synchrotron, nous donnons des exemples originaux qui illustrent les possibilités nouvelles pour les études de croissance cristalline : caractérisation de cristaux produits pour des applications, tels les tri-cristaux de glace que l'on fait pousser pour des études de déformation mécanique, SiC, silicium monocristallin pour des cellules solaires photovoltaïques, des études in situ et en temps réel de la croissance de quasicristaux (AlPdMn), et la tomographie ultrarapide pour l'étude de la croissance de dendrites dans des alliages métalliques.

© 2012 Académie des sciences. Published by Elsevier Masson SAS. All rights reserved.

* Corresponding author.
  E-mail address: tamzin.lafford@esrf.fr (T. Lafford).

1. Introduction

When dealing with non-uniform samples, imaging techniques are needed because these samples produce an inhomogeneous response to the beam, resulting in *contrast* within the detected image. X-ray imaging started with the discovery of X-rays, allowing, through absorption radiography, the visualisation of the volume of specimens opaque to other probes. For several decades, this was the only form of X-ray imaging. About fifty years ago, Bragg diffraction imaging developed into practical use. This "diffraction topographic" approach applies to single crystals and basically consists of mapping the intensity and direction of the locally Bragg diffracted beams. It reveals defects in the bulk of single crystals, and helped to develop production of large, practically perfect crystals for the microelectronics industry. These techniques extended beyond semiconductor crystals, and are useful for investigating induced or growth defects and distortions. Their range of applications dramatically grew when synchrotron radiation (SR) became available to condensed matter scientists, including then topics such as in situ crystal growth, defect nucleation and movement, and phase transitions.

All the X-ray imaging methods benefited from the use of SR, and in particular from the features of modern, "third generation", SR machines. Real time and high spatial resolution experiments are nowadays routinely performed, and the high coherence of the beam allows exploitation of a novel form of radiography, in which contrast arises not only from absorption differences but also from phase variations across the transmitted beam. Absorption and phase microradiography and its three-dimensional companion, microtomography, provide useful information on crystal growth-related features (porosities, inclusions, areas with different composition, dendritic growth, etc.). The spatial resolution of these two or three-dimensional "parallel beam" imaging techniques is today in the μm range. In addition, the highly brilliant sources of modern SR facilities, coupled with new X-ray optics, allow microbeams in the sub-μm range to be achieved. These new devices enable nano-imaging to be performed, with a spatial resolution presently around 50 nm. This leads to another type of imaging through the use of X-ray nanobeam-based scanning approaches, probing for instance the fluorescence or the absorption near the absorption edges.

The initial part of this article briefly deals with the developments of SR based X-ray imaging techniques that may be of interest for crystal growth. These include firstly transmission (absorption and phase) imaging, in its two- or three-dimensional ("microtomographic") forms, and secondly microbeam techniques (imaging, fluorescence, diffraction). Then Bragg diffraction imaging ("topography"), i.e. a set of techniques that is specific to the investigation of inhomogeneities in single crystals is briefly described.

In the final, and main, part of the present article we give recent examples showing the capabilities of these techniques, and their combinations, to help solve various topics of interest for crystal growth. The first example is the way simple white beam diffraction imaging characterisation helped improve the crystal growth procedure to obtain high crystalline quality ice grains. The second example shows how "section" diffraction imaging allowed the visualisation in the bulk of growth defects in SiC ingots. The combination of radiography and diffraction imaging gave clues to the elusive problem of the growth of quasicrystals. The combination of diffraction imaging and microfluorescence constitutes an important tool for the investigation of the properties of silicon grown for photovoltaic applications. Lastly, very fast microtomography has been used to study the dendritic growth of Al based metallic alloys.

2. Imaging techniques for crystal growth studies

2.1. Absorption and phase radiography and tomography

The absorption of X-rays is usually described by the absorption coefficient μ, such that the intensity I_T after transmission through the sample may be written as:

$$I_T(y, z) = I_0(y, z) \exp\left[-\int\limits_{\text{path}} \mu(x, y, z)\, dx \right]$$

where I_0 is incident beam intensity.

Computer-assisted tomography provides the three-dimensional (3D) absorption image of a bulky object from the two-dimensional (2D) images (radiographs) recorded at various angular positions of the object, processed using appropriate algorithms and software. From the reconstructed 3D data, any virtual slice, or perspective renditions, of the object can be obtained.

Laboratory microtomographic instruments, exhibiting a spatial resolution in the μm range, have been developed over recent years and are commercially available. However, the best quality images, in terms of signal-to-noise ratio and spatial resolution, are obtained on instruments located at SR facilities.

Fig. 1 shows the principle of the most commonly used SR-based radiographic and tomographic acquisition methods. The experimental conditions are optimised through the use of either monochromatic ($\Delta E/E \approx 10^{-4}$–$10^{-2}$) or "pink" ($\Delta E/E \approx 10^{-1}$, E being the X-ray photon energy) beams, depending on the aim of the experiment and the way the data has to be analysed to extract relevant information. The beam can be considered as parallel, the source being situated far from the sample (150 metres at ID19, one of the imaging beamlines of the ESRF). This "parallel beam" approach implies that no magnification is obtained, and the spatial resolution mainly results from the effective pixel size of the detector. However,
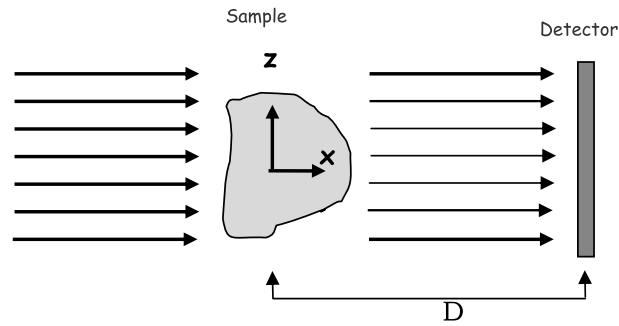
Fig. 1. Diagram of radiography: the contrast mechanism can be absorption or, when dealing with a coherent beam, phase. A 3D image (tomograph) can be obtained by rotating the sample in the beam, recording a series of radiographs, and using appropriate software to reconstruct the 3D volume.

this configuration exhibits the advantage that all the radiographs, recorded on the 2D detector, obtained by rotation of the sample about z, are such that each slice, at a given height z, is independent of the other slices. The 3D problem reduces, in this parallel geometry, to a sequence of 2D calculations. Several reconstruction algorithms, such as the filtered back-projection (FBP) or the algebraic reconstruction techniques (ART), have been developed. Their mathematical description is beyond the scope of the present paper, but can be found in [1,2].

The X-ray beams produced at modern synchrotron radiation facilities exhibit a high degree of coherence. This is due to the very small angular size α of the source as seen from a point in the specimen ($\alpha \sim$ μrad range), leading to a large lateral coherence L_c of the X-ray beam with wavelength λ ($L_c = \lambda/2\alpha$). L_c is about 100 μm ($\lambda = 1$ Å) at the 150 m long ESRF ID19 beamline.

The interaction of X-rays with matter can be expressed through the complex refractive index $n = 1 - \delta + i\beta$ that describes both absorption ($\beta = \lambda\mu/4\pi$) and the phase change $\Delta\phi$ ($\Delta\phi = 2\pi\delta t/\lambda$) with respect to a path t in vacuum. The decrement δ of the refractive index, in the 10^{-5}–10^{-6} range, is, within a very good approximation, proportional to the electronic density in the material, hence to its mass density. The passage of an X-ray beam through a sample entails a phase shift $\Delta\phi(y, z)$ variable over the cross-section of the beam if the beam has passed through a sample with inhomogeneous thickness and/or structure.

Modern SR beams allow, with great instrumental simplicity ("propagation" technique, [3–5]), the phase variations of hard X-rays to be revealed, be it in simple radiography or in tomography. From the optical point of view, the effect used to change the local phase variations into intensity variations can be described in terms of Fresnel diffraction, i.e. the interference, at finite distances, of parts of the beam that undergo different phase shifts, but are mutually coherent. The great advantage of using phase contrast is the increased sensitivity it provides. This corresponds to the fact that $\delta \gg \beta$ (10–1000 times bigger) in the hard X-ray range ($E > 6$ keV). This increased sensitivity allows visualisation of tiny objects such as cracks, pores or regions exhibiting even a weak ($\sim 1\%$) density variation with respect to the matrix.

In practice, obtaining a phase-sensitive image involves merely setting the detector at a distance D from the specimen (Fig. 1) of the order of 10^{-1} m. Phase variations across the beam exiting the sample lead to variations in intensity, hence to contrast, provided the phase has a two-dimensional Laplacian $\nabla^2\phi(y, z) \neq 0$. An absorption image is obtained if D is small (10^{-3} m range). Phase contrast shows up, for increasing distance D, first through the appearance of a black–white line at the phase discontinuities ("edge enhancement"), then a more and more obtrusive Fresnel fringe system ("holography") which progressively changes towards the Fraunhofer regime. These fringes contain quantitative information about $\phi(y, z)$. A "holographic" algorithm for phase retrieval, based on images recorded at several distances, has been produced by Cloetens [6]. Other algorithms, with additional approximations, like the ones of Paganin [7], were elaborated to reduce the number of distances and the calculation time: they have proved to be very efficient, even beyond what was initially considered to be their domain of applicability. Phase contrast imaging was extended to 3D, and opened up access to the spatial distribution of δ, and hence of density.

2.2. Microbeam based X-ray imaging techniques: Nano-imaging

The absorption or phase-based imaging techniques described above cannot provide information on the local elemental composition and/or structure. This requires combining scattering measurements with scanning of the sample. The X-ray beams produced at modern SR sources can, because they originate from a very small source, be focused into a very fine spot (0.05–1 μm range) with extremely high intensity. Various focusing elements are currently used to produce small section beams: the main ones are compound refractive lenses and Kirkpatrick–Baez ("KB") focusing mirrors or multilayers ([8], and references therein). It is then possible to scan the sample and collect quantitative information, which is an "image" when displayed in the form of a (y, z) map corresponding to the position of the beam on the sample.

X-ray microfluorescence (μ-XRF) allows mapping of the presence and concentrations of elements in the sample. A beam of energy E_0 is focused on a small area of the sample. A solid-state detector is set at 90° with respect to the incident beam.
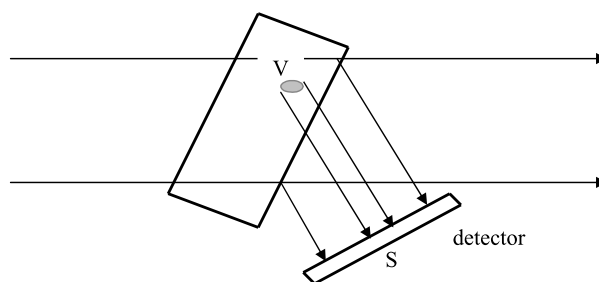
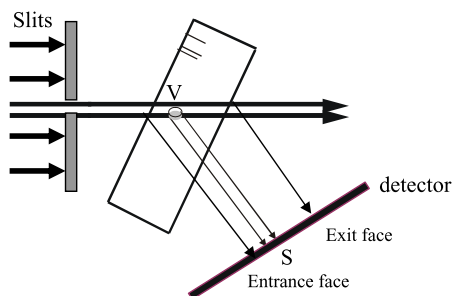**Fig. 2.** Bragg diffraction imaging (see text).

Fig. 3. Principle of "section" diffraction topography. With white beam, any sample angle produces diffraction. With a parallel monochromatic beam, the sample must be set accurately at the appropriate Bragg angle in order to obtain a diffraction image.

A given element produces fluorescence with a characteristic energy E_f. The spatial resolution is, in the hard X-ray range, mainly determined by the spot size.

Fluorescence is not the only quantity that can be mapped: wide angle diffracted X-rays [9,10], or small-angle scattered X-rays, absorption, or secondary electrons, provide additional information. Scanning imaging simultaneously exhibits high spatial resolution (sub-µm scale in the hard X-ray range) and elevated chemical selectivity. Local (at the sub-µm level) information on different chemical states within systems having the same elemental composition is therefore possible.

2.3. X-ray Bragg diffraction imaging

X-ray Bragg diffraction can be used to produce images of crystalline materials. When dealing with polycrystalline materials, a series of related techniques (such as diffraction contrast tomography, DCT [11]) was developed to provide the shape, orientation and state of distortion of the different single-crystal grains. When dealing with a single crystal (or a single crystalline grain) Bragg diffraction imaging techniques (diffraction topography [12], rocking curve imaging [13]) provide, through the local variations of the intensity or direction of the diffracted beam, information on crystal distortion and defects (dislocations, crystallographic twins, inclusions, etc.) [14–16].

Fig. 2 schematically represents the concept of all the diffraction imaging methods. The crystal fulfils the Bragg law $2d \sin \theta_B = \lambda$ and diffracts a fraction of the incoming beam, which is recorded on a position sensitive detector (X-ray films, or, increasingly, CCD cameras equipped with a high resolution scintillator). If a small volume V behaves differently from the matrix, intensity variations ("contrast") can be produced on an area S of the two-dimensional image generated by the diffracted beam.

Defects can be observed because they entail a distortion (lattice rotation $\delta\theta$ and/or lattice parameter variation $\Delta d/d$) of the crystal lattice. Bragg diffraction imaging may be used either in *transmission* or in *reflection*. In both cases the crystal should, when using white beam, ideally be of the order of, or thicker than, the extinction length Λ_0. This extinction length can be viewed, (1) in the reflection case, as the "penetration depth" required, in a perfect crystal, to diffract all the components of the incident beam able to participate in Bragg diffraction, and (2) in the transmission case, we will mainly consider in the present paper, as about twice the distance necessary for most of the energy participating to the diffraction process to move from the transmitted to the diffracted direction. The values of Λ_0 are typically in the 1–100 µm range.

When the beam is extended, as shown in Fig. 2, the depth information can be lost because the 3D crystal is projected onto a 2D detector. A way to overcome this limitation consists in restricting by slits the incoming beam to a small width (typically 10–50 µm) in the scattering plane (Fig. 3). In the same first approximation this produces an image of those defects intercepted by the blade-shaped incident beam, hence the name "section" topograph.

In section topography, the positions of the defect images within the global image can be used to extract the depth of these defects in the crystal, one edge of the image corresponding to the entrance surface of the sample, the other to the exit surface. In very good crystals, with small or moderate absorption, interference fringes ("Kato's fringes") are observed in
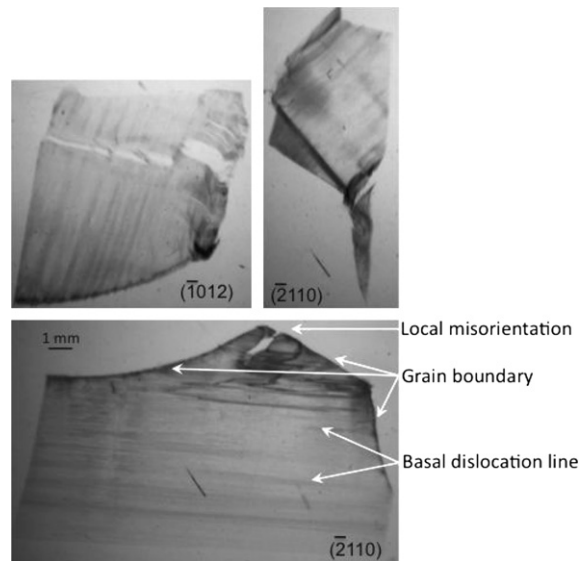
Fig. 4. Three grains of 1 mm thick ice tri-crystals imaged with polychromatic light; the sample was obtained during one of the first growths of this project.

the section image. These fringes are very sensitive to crystal distortion, and their modification is one of the first indications of a departure from a perfect crystal.

3. Examples of the application of synchrotron radiation imaging techniques to crystal growth studies

Synchrotron radiation is now widely used for X-ray imaging. The short exposure time (a fraction of a second for a diffraction image, a few ms for absorption or phase radiography) allows investigation of evolving phenomena. Specific sample environments (cryostat, furnace, electromagnetic field, strain device) can be added for each particular experiment.

We present, in this section, some examples of the application of synchrotron radiation imaging to topics related to crystal growth, performed on the ESRF beamlines BM05, ID15, ID19 and ID22. They go from the simple characterisation after growth, by both projection and section topography, to improve the growth procedures, to more complex applications, involving the simultaneous use of several techniques, and/or in situ, real time experiments during the growth process.

3.1. Ice crystal growth for deformation studies

To understand the early stages of plasticity in crystalline materials it is necessary to study the movements and interactions between dislocations, and to follow the evolution of the dislocation density. These phenomena are particularly pronounced in the neighbourhood of grain boundaries. It is therefore essential to start with high quality grains with a low dislocation density. Methods for growing high quality single crystals of ice have been implemented: they are based on the well known Bridgman or Czochralski techniques, and allow dislocation densities as low as 10^6 m/m^3 to be achieved [17].

However, ice in the natural environment is mostly polycrystalline. Our first task was therefore to work out a growth method for ice multi-crystals and a protocol for specimen preparation, as simple as possible, resulting in ice grains with a low initial dislocation density. The idea was, once this step achieved, to extract "model samples", ice tri-crystals, and to follow them during their deformation, in particular near grain boundaries and the triple junction of the three grains.

A convenient way of obtaining large multi-crystals (i.e. > 1 cm in diameter, with real grain boundaries) is to mimic the formation of natural lake ice. This type of ice grows under a vertical temperature gradient, with the air at the lake surface colder than the bottom layer of water. Under such conditions the crystals tend to grow as columns elongated in the direction of the temperature gradient. To reproduce lake ice growth, a tank with insulated walls (50 cm high) and a metallic bottom (30×30 cm^2) is filled with water (kept at 1 °C). This is set on a refrigerating table with adjustable temperature, which allows the creation of a vertical temperature gradient. Both are placed in a cold room at a temperature between 0 and +1 °C. Owing to the lateral insulation of the tank, the temperature gradient is close to uniform in the horizontal plane, leading to a quasi-planar freezing front. The conditions are thus similar to those of natural lake ice growth, although the temperature gradient is reversed. However, ice tends to occupy a greater volume than water during the phase transition, and because the walls of the tank prevent ice from expanding laterally, internal stresses may develop during growth, which are detrimental to the quality of the crystals. This quality was assessed by estimating the dislocation density imaged by SR X-ray diffraction topography. Fig. 4 shows the crystalline quality obtained in the first growth trials at the start of the study. Dislocation densities and local misorientations were quite significant.
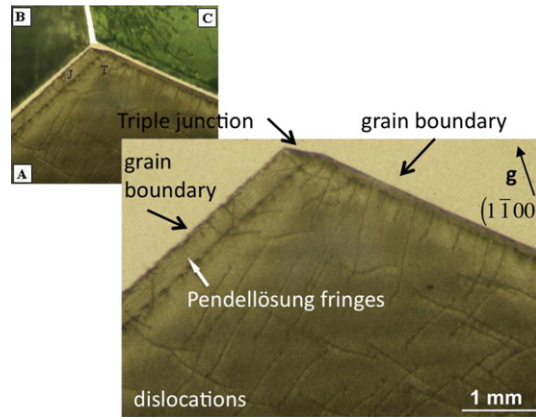
Fig. 5. Sample obtained with the improved protocol described in this paper. The three grains, which exhibit high crystalline quality, are presented on a "composite" diffraction image, which corresponds to Bragg reflections different for each grain. The crystalline quality, in particular near the grain boundaries, can be observed on the magnified figure of the lower grain, where interference fringes ("equal thickness") are observed on the inclined boundary between grains.

During this project, different conditions for growing, specimen shape machining, preservation and storage time prior to testing were tested. The experimental protocol was improved by an immediate characterisation of the samples by SR topography, until an efficient, reproducible growth protocol was established.

The essential steps of the procedure are as follows:

– A basic step toward the crystalline quality is to use water which is as pure as possible. To grow our crystals we use deionised and demineralised water from a commercial system (Milli-Q, resistivity ≈ 20 MΩ cm^{-1}).
– Since the quality of ice depends on the quality of the seed crystal [18] we prefer to let a spontaneous germination occur when the cold water (1 °C) fills the bottom of the tank (−5 °C).
– A minimum of defects in ice is obtained when the temperature gradient is low enough to keep the growth rate as slow as possible. The slowest rate tested was 8 mm per day (an order of magnitude smaller that what is proposed in the literature to obtain "quasi-perfect" crystals).
– To prevent the formation of air bubbles in the ice, the best solution would be to use de-aerated water and to isolate the water surface from the ambient air during growth. We have adopted a simpler solution, which consists in emptying and refilling the tank with cold water (1 °C) every 24 hours: doing so prevents the concentration of dissolved air at the freezing front (and eventually the concentration of other contaminants from the cold room) and results in perfectly transparent ice (i.e. with no bubbles visible to the eye).

This optimised procedure allows ice blocks ($30 \times 30 \times 30$ cm^3) to be obtained that contain large columnar grains (up to 80 mm in diameter) elongated parallel to the temperature gradient with their *c*-axes roughly perpendicular to the columns. Because the ice samples are to be observed during their deformation under plane strain conditions, they are given a parallelepiped shape. These rectangular plates are 1 to 4 mm thick and approximately 17 mm × 21 mm in the plane direction. They are cut perpendicular to the direction of the ice columns and their final shape is achieved by machining with a milling machine in a cold room at −10 °C. The 1 mm thick specimens were used to check the crystalline defects by SR white beam topography. The thicker specimens were observed in the bulk by three-dimensional rocking curve imaging (using thick specimens allows the perturbations from the surface defects created by the machining process to be avoided).

Fig. 5 shows Bragg images ("topographs") obtained with SR polychromatic light of the grains of a tri-crystal sample 1 mm thick. Grain boundaries and the triple junction can be seen in projection. The dislocations appear as almost straight dark lines in the crystal volume. There are few in number, even in the vicinity of the grain boundaries and of the triple junction. Direct counting and estimation by Ham's method [19] are in agreement to give a dislocation density of about 10^6 m/m^3. This dislocation density is about two orders of magnitude lower than those determined in natural ice. Kato's equal thickness (or "Pendellösung") fringes can be seen in the projected thickness of the grain boundary, this attesting the very high crystalline quality obtained with the proposed, simple, protocol. This allows observing individual dislocations and following the evolution of the dislocation density during the deformation, even in the most problematic (and interesting) regions, in the neighbourhood of the grain boundaries.

3.2. Investigation of SiC as-grown ingots by white beam X-ray section topography

The large potential of silicon carbide (SiC) as a material for high-temperature and high-power semiconductor devices is still limited by the influence of the grown-in structural defects on device performance. The aim of our experiment was
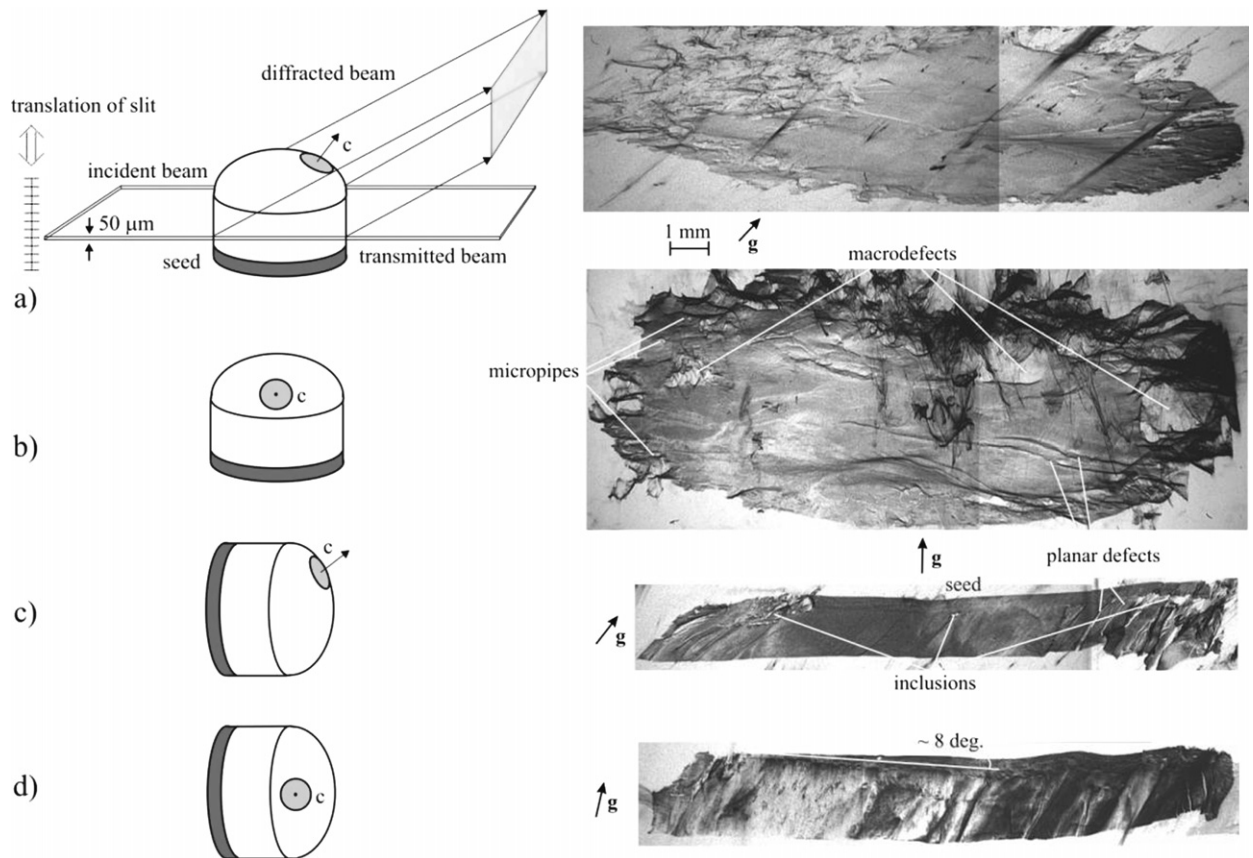
Fig. 6. (a) Experimental arrangement for section topography; the incident beam position on the sample is adjusted by displacing the slit. (a–d) Four geometries of positions of the SiC ingot and the beam are presented, with the corresponding section topographs; the facet perpendicular to the *c*-axis is indicated by the grey circle/ellipse. The vector **g** is the projection of the diffraction vector on the detector.

to characterise defects and their propagation during crystal growth inside bulky ingots of SiC without slicing them, and to establish links between growth conditions (seed, temperature gradient, gas pressure, etc.) and observed defects.

4H-SiC ingots were grown by sublimation physical vapour transport with in situ sublimation ("modified Lely method") [20]. Cylindrical crystals with diameter of up to 35 mm and height of about 12 mm were obtained. The main crystal was surrounded in the radial direction by a polycrystalline region about 5 mm thick. The ingots were cut out from their carbon crucibles and no additional preparation was performed. The 4H-SiC ingot we investigated contained typical defects such as polytype inclusions, misoriented regions, micropipes (giant screw dislocations with a hollow core), dislocations, grain boundaries and macrodefects (holes produces by local sublimation of the seed).

White beam section topographs were recorded, as schematically indicated in Fig. 6a, for different positions on the sample (Kodak Industrex SR films, typical exposure time $\sim$ 10 s, crystal-to-film distance $\sim$ 20 cm, spatial resolution $\sim$ 5 μm). This was performed for four distinct geometries, schematically depicted in Fig. 6. The results obtained by this procedure allowed the determination of the 3D shape of the defects inside the ingot. Each of the images showed the defects contained in the "virtual" slice corresponding to the intersection of the crystal by the beam. This allowed the superposition of the images of defects of a large crystal volume onto a 2D detector to be avoided, an approach that is particularly useful when the crystalline quality of the sample investigated is not very high, which was our case.

The 'horizontal' sections (Figs. 6a and 6b) were performed with the main axis of a cylindrical ingot vertical and correspond to the areas formed approximately at the same moment of the crystal growth. The *c*-axis direction is indicated for each of the positions. However, the 'vertical' sections (Figs. 6c and 6d) were carried out with the main ingot axis laying along the incident beam direction: they allowed visualisation of the propagation of a given defect during the crystal growth. The images shown in Fig. 6 correspond to the central part of the ingot, the other sections recorded at other positions not being presented, but they were of course included in the analysis and support the resulting observations and conclusions.

Due to the geometrical projection onto the detector, the horizontal sections have an elliptical shape, while the cross section of the sample with the incident beam is circular. The presence of the polycrystal surrounding the main crystal leads to deformation of the ellipse and produces additional contrast at the periphery of the ingot image. Macrodefects, inclusions of other polytypes and micropipes are observed mainly at the periphery of the images 6a and 6b, the central part of the ingot being of higher crystalline quality. An additional feature is observed in Fig. 6b: lines nearly perpendicular to the
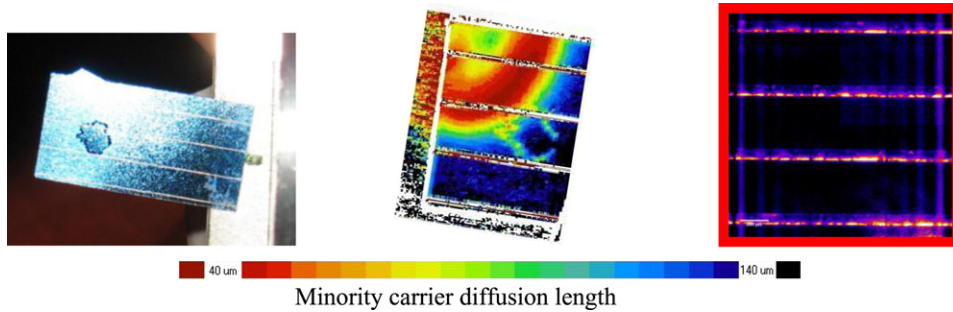
Fig. 7. Left: photograph of a mono-like solar cell exhibiting a crystallographic twin surrounded by smaller grains. The front surface (shown) is textured and anti-reflection coated before deposition of the thin Ag contact lines visible in the picture. Middle: corresponding LBIC map of part of the sample – the positions of the grains surrounding the twin are easily identified. Local misorientation of the surface of these grains may explain the difference in PV performance here, but does not explain the poorer performance in the red region above. Right: section topograph of an area of the sample in the red zone, $\sim 1.5 \times 1.5$ mm^2 – the effect of the Al backplane on the silicon shows up at the lower edge of each section. (LBIC data by courtesy of Nelly Plassat, INES. For interpretation of the references to colour in this figure legend, the reader is referred to the web version of this article.)

diffraction vector projection **g**, which are curved when the crystal matrix is deformed, exhibit white or black contrast and display a higher density when closer to the seed.

The vertical section topographs show the crystal growth from the seed to its natural top surface. The seed–crystal interface is hardly visible on both vertical sections of Figs. 6c, 6d, indicating a smooth start to the crystal growth. Inclusions of another polytype, 6H-SiC or 15R-SiC, near to the seed can be observed in Figs. 6c and 6d, mainly at the side of the images corresponding to the periphery of the ingot. Fig. 6d indicates that the polytype inclusions start to grow from one side of the ingot and propagate, with an angle $\sim 8°$ with respect to the horizontal ingot axis, until they reach the other side of the ingot. These inclusions induce planar defects that grow parallel to the vertical ingot axis up to the natural crystal surface, and originate the lines observed in Fig. 6b, described above.

The systematic investigation of several 4H-SiC ingots indicates that these polytype inclusions at 8° are generally reversible. The defects generated concern often only a part of the crystal; however they deteriorate considerably the general crystalline quality. This polytype switching originates from the 8° off-axis orientation of the seed. If at the beginning of the growth process some instability appears, a 6H-SiC or 15R-SiC single-crystal grain can be created outside the seed. In the case when this grain is located at the right extremity of the seed and has the same orientation as the 4H main crystal, it starts to grow and progressively covers a part of the 4H crystal. As during further crystal growth the process parameters such as pressure or temperature are favourable for the growth of the 4H polytype, the conversion back to 4H-SiC appears. However, this re-conversion provokes the occurrence of distortions in the new grown crystal, such as grain boundaries.

The systematic study, by SR section topography, of various 4H-SiC ingots allowed a correlation to be established between the seed orientation, growth conditions and occurrence of the 6H-SiC or 15R-SiC inclusions, associated with planar defects that deteriorate the overall crystalline quality. Once the instabilities at the beginning of the growth process were successfully reduced, the useful volume of the grown crystals was considerably increased [20].

3.3. Crystalline silicon (c-Si) for solar photovoltaic cells

Microelectronic grade silicon provides monocrystalline photovoltaic solar cells with the highest efficiencies but also the highest prices. This is not only affected by the quality of the silicon feedstock and the slow and careful crystallisation process, but also by the effect of demand for raw material on the market. More rapid growth processes using "dirtier" feedstock are therefore the subject of ongoing research. While industrially-processed monocrystalline silicon (mono-Si, such as is produced for the microelectronics industry) solar cells typically deliver ~ 18–19% efficiency and lab-based examples have reached 24–25%, typical commercial efficiencies obtained from multi-crystalline silicon (mc-Si) are ~ 14%. However, "mono-like" silicon can deliver ~ 17–18.5% efficiency – a promising competitor to mono-Si.

Mono-like Si is grown from metallurgical grade (MG), upgraded metallurgical grade (UMG), or solar grade (SoG) feedstock on monocrystalline seed crystals. Placing several seed crystals side by side in a crucible enables ingots up to 380 mm $\times$ 380 mm across to be grown in a pilot line, and up to 840 mm $\times$ 840 mm in an industrial furnace. Wafers cut from the lower part of the ingot, nearer the seed, are highly mono-like, while twins and grains tend to appear higher up. Since the presence of dislocations, impurities and grain boundaries affect photovoltaic performance, X-ray imaging and mapping techniques combined with mapping of such parameters as minority-carrier diffusion length by light beam induced current (LBIC) give important information on the correlation between defects and PV performance. When micro-X-ray beams are used, such as in μ-X-ray fluorescence measurements, the X-ray beam induced current (XBIC) may be measured simultaneously, giving an exact correlation between the two maps produced [21,22]. Figs. 7 and 8 are examples of combining techniques: Fig. 7 shows a sample, the LBIC measurements indicating regions of good and poor PV performance, and a section topograph showing the distortions associated with the Al backplane on the Si, which may be correlated to the PV performance; Fig. 8
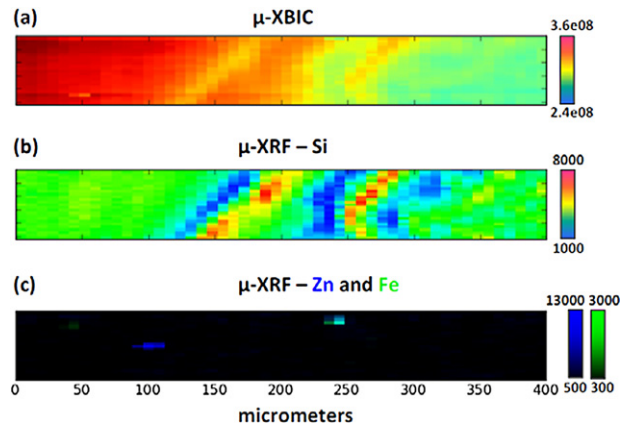
Fig. 8. Simultaneous μ-XBIC and μ-XRF measurements across a grain boundary, showing the effect of the topology of the Si surface, which affects the amount of signal measured, and the presence of localised Zn and Fe contamination which appears to have agglomerated at grain boundaries. Data collected at ID22, ESRF; with special thanks to Julie Villanova, ESRF.

shows simultaneous μ-X-ray fluorescence and μ-XBIC measurements. X-ray measurements may be taken on bare wafers or prepared cells.

3.4. Real time investigation of columnar and equiaxed growth of quasicrystals

The 2011 Nobel prize in chemistry was awarded to D. Shechtman for the discovery of quasicrystals (QC) in AlMn alloys [23]. QCs are solids that display long-range rotational order with symmetries long considered as strictly forbidden in nature. They also exhibit many specific properties that have motivated engineers to use them as new materials (e.g. for advanced surface coatings or catalysis). The main challenges of QC physics are still to elucidate why they form and how the quasiperiodic order can extend up to the centimetre size of the grains routinely grown nowadays. It is therefore critical and timely to deepen the understanding of the dynamics of QC formation and growth from the liquid alloy, in particular to clarify the growth mechanisms, in which the peculiar QC structure is continuously constructed.

Solidification experiments were carried out at the ID19 beamline of the ESRF. Two 700 μm-thick sheets, 40 mm long and 6 mm wide, were prepared by grinding rods of $Al_{72.4}Pd_{20.5}Mn_{7.1}$ alloy, whose composition is known to give the icosahedral QC phase [24]. These sheets were first melted, and then solidified at various pulling velocities (0.4–3.6 μm/s) under a temperature gradient of 35 K/cm. Quasicrystallinity of the solid structure was repeatedly checked by indexing Laue patterns recorded after cooling, while energy-dispersive spectrometry (EDS) was used for supplementary control to check if the measured composition corresponded to icosahedral AlPdMn on the phase diagram.

A key issue is the (quasi)crystallographic quality of this new class of materials. In order to investigate the grain quality during its growth, dedicated experiments were carried out. In the experiment presented in this paper, which is representative of most of our experiments, a sharp increase of the pulling rate was applied from 1.2 to 3.6 μm/s at a given time (chosen as the reference time in Fig. 9) to provoke the columnar-to-equiaxed transition [25]. The main goal was to follow in situ the growth of an equiaxed grain, from the very early stages following its nucleation, up to a millimetre size, with a combination of topography (Figs. 9a to 9e) and radiography (Figs. 9f to 9h) techniques [26]. Firstly, in situ X-ray radiography unambiguously unveils the faceted growth of the solid–melt interface in QC solidification, as suspected. Secondly, the good contrast between the dark solid and the grey liquid means that the solid is denser than the liquid phase. This observation is an unambiguous experimental proof of the non-congruent solidification of AlPdMn quasicrystals, with rejection of aluminium in the surrounding melt which induces a gradual decrease of the liquid density as confirmed by further EDS measurements. It is worth mentioning that the aluminium rejection during the growth process of a single grain is at the origin of a self-poisoning effect, due to solutal convection that leads to asymmetric growth of the different facets [25]. Thirdly, growth kinetics in quasicrystal growth are expected to be very slow, due to uneasy attachment of the building element in the melt to the solidification front. By measuring the front recoil caused by the jump of the pulling velocity, we were able to deduce an experimental estimate of the kinetic coefficient, $\mu = 0.9$ μm s^{-1} K^{-1} [25]. This value is comparable to the ledge growth kinetics of semiconductors and oxides (for instance 0.826 μm s^{-1} K^{-1} for $Bi_4Ge_3O_{12}$ [27]), definitely much slower than the solidification kinetics of pure metals but not as sluggish as admitted (0.9 ms^{-1} K^{-1} is two orders of magnitude larger than the value derived by Dong et al. [28]).

The topographs of the QC grain (Figs. 9a to 9e) also exhibited faceted growth, but not as clearly as the radiographs (Figs. 9g and 9h). This means that there were strong distortions and/or defects in the grain (estimated to be, in "dislocation units", bigger than $\sim 10^5$–10^6 cm/cm^3). This observation was true even in the very early stages following grain nucleation (Figs. 9a and 9b). These distortions could be caused either by the fact that the grain nucleated on the crucible wall and remained stuck (which created stresses in the growing solid), or were intrinsic to the QC growth process. In our experiments, it was not possible to discriminate between those effects. However, all topographs recorded during the solidification phase
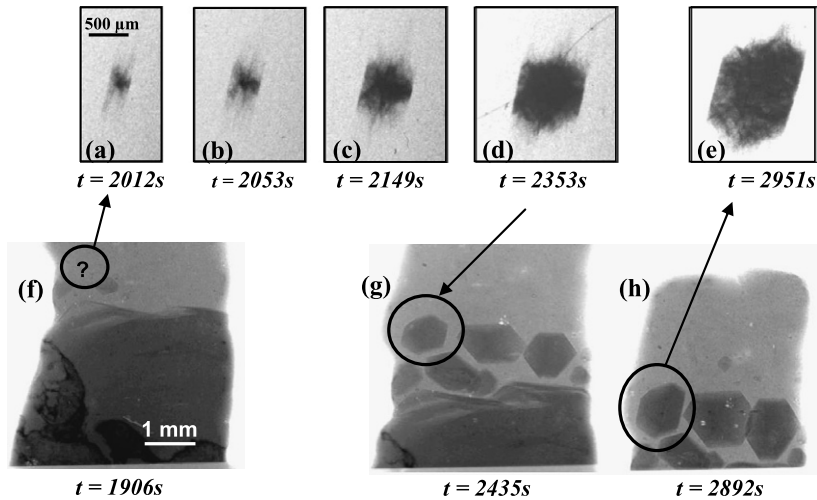
Fig. 9. Topographs (a–e) and radiographs (f–h) of a quasicrystal grain during the growth process in a temperature gradient of 35 K/cm, $t = 0$ s is the moment when the pulling rate was changed from 1.2 to 3.6 µm/s.
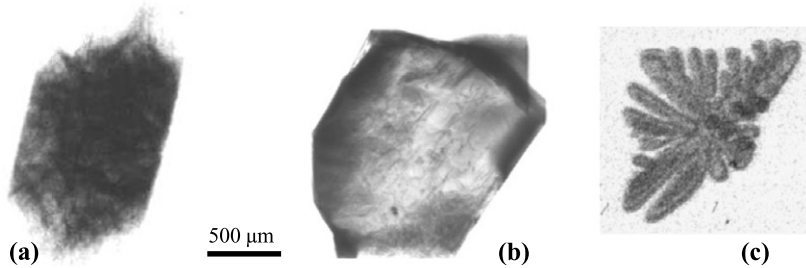

Fig. 10. Topographs of (a) QC grain during the growth process, (b) QC grain recorded by Gastaldi et al. at room temperature [29] and (c) Al dendritic grain stuck on the crucible wall during the growth process, showing Kato's equal thickness fringes, signature of a very high level of crystalline perfection [26].

showed constrained and distorted QCs, whereas Gastaldi et al. [29] obtained QC with very high crystallographic quality at room temperature (Figs. 10a and 10b). This observation is quite surprising, if we assume that crystalline structures are generally more distorted at room temperature than during the growth process, due to thermal stresses [30]. For instance, in the case of dendritic growth of an aluminium grain stuck on the crucible wall (Fig. 10c), Kato's equal thickness fringes are visible, and confirm its very high crystalline quality [26]. These observations suggest that the distortions in the growing QC grain could be intrinsic, associated with the difficult attachment of the building element or cluster to the solidification front. These distortions may then be relaxed in the subsequent stages. The old question of pores (origin and formation), which is generally admitted as one of the important special features of QC, might be related to the relaxation process of such distortions created during the QC solidification phase [31].

3.5. Real time investigation of the dendritic growth of an Al–Cu alloy

The solidification of metallic alloys is a 3D phenomenon. In order to study it in situ, very fast microtomography is required. As an example, Fig. 11 presents the necessary minimum acquisition time in seconds as a function of the volume fraction of the solid phase for various cooling rates in an Al–20 wt% Cu. It was assumed, for the sake of simplicity, that the solid phase is spherical with a solid density of 1000 grains per mm³. This is of course a rough estimate but it provides information that corresponds to what has been observed in practice.

It can be deduced from this figure that it is not possible to perform 3D in situ tomography with scan times longer than 100 seconds without reducing the cooling rates to unrealistic values. Furthermore, if one wants to study the early stage of solidification with reasonable cooling rates (around 1 °C/s), it means that the acquisition time should be less than 1 second. So fast acquisition cameras and, of course, high photon flux is required, which is only available at modern synchrotron sources. In order to get a suitable field of view (at least 1024×1024 pixels) with a spatial resolution of the order of 2 µm, present CCD cameras limit the acquisition time to approximately 15 seconds while CMOS cameras allow acquisition times as fast as 0.2 second to be attained. Therefore these CMOS cameras are mostly used.
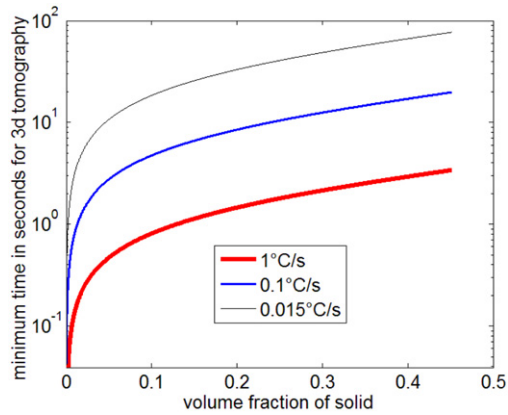
Fig. 11. Minimum acquisition time in seconds for 3D tomography as a function of solid volume fraction for an Al–20 wt% Cu alloy at various cooling rates.
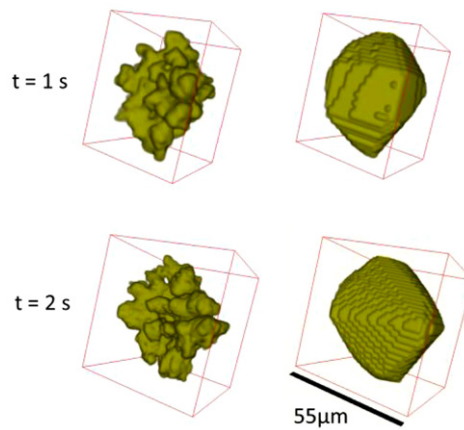
Fig. 12. 3D rendering of the dendrite and its envelope for two solidification times (1 s and 2 s).

3D in situ solidification experiments also require an adapted sample environment, in order to heat and cool the sample. This sample environment can be a classical furnace, such as has been used in several solidification studies at the ESRF [32–36] or, more recently, a laser furnace as developed at the SLS [37].

We performed, at ID15 (ESRF), ultra fast tomography with a CMOS camera during the solidification of an Al–20 wt% Cu alloy, chosen to maximise the contrast between the solid and the liquid phases. Six hundred projections were used to obtain a scan and the exposure time for one radiograph was 0.25 millisecond: therefore the total time to acquire 600 projections was 0.15 second. The optics used were set to a pixel size of 2.2 μm. Details of this experiment and its analysis can be found in [38]. The sample (diameter 1.5 mm and height 1 mm) was heated in a small furnace in order to be fully liquid. The furnace was quickly removed and images were taken during 10 seconds which represents approximately 70 scans. The cooling rate was estimated from the images to be 5 °C/s. Thanks to 3D image analysis, it is possible to extract several parameters for each dendrite such as the volume, surface, solidification front, envelope and their positions at the early stage of solidification (from a solid fraction of 0.05) and thus these data could be compared to numerical simulation of equiaxed dendritic growth. In Fig. 12, where the solidification times are 1 and 2 seconds, the envelopes were obtained using 3D convex hull [39,40]. The volume ratio between the dendrites and the envelope is approximately 0.43 after 1 s of solidification and decreases to 0.38 when the solidification time is 2 s. Fig. 13 illustrates the solidification front of one dendrite which was determined with the local bounding box of the dendrite in its principal directions (local *bx*, local *by*, local *bz*). It can be seen that the solidification front increases linearly with a slope of 7–10 μm/s and then saturates after 2 seconds, which corresponds to a solid fraction of 0.15. This can be explained by the interaction of dendrites, which lower the solidification front propagation, as has been observed using radiography [41,42]. This figure indicates the potential of the imaging experiments, which provide not only a first qualitative visualisation of the phenomena, but can be exploited to progress, quantitatively, in understanding them theoretically.
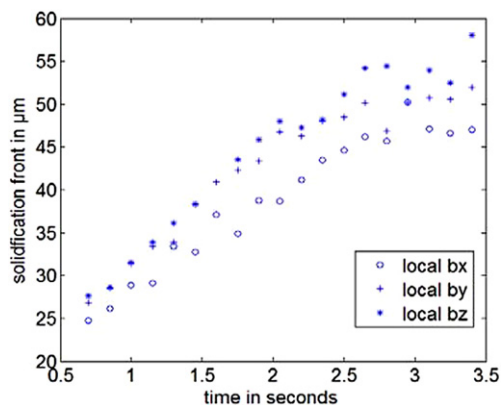
Fig. 13. Solidification front of one dendrite versus solidification time: solidification front is obtained by the local bounding box in the three principal directions of the dendrite.

4. Conclusion

The above examples, as well as those presented in a previous review [43], show that synchrotron radiation-based imaging techniques are very useful tools for characterising crystals and growth-related features and providing original information on the growth process when observed in situ. The techniques already used include absorption imaging (radiography and tomography), Bragg diffraction imaging and scanning imaging (μ-XRF in the present paper). We can anticipate that the increasing capabilities of phase imaging, which are used for many scientific topics, will surely apply to crystal growth processes in the near future. These techniques are in constant evolution, and spatial and temporal resolution improvements, new tools for image processing, and extension to new topics, are observed recurrently.

References

[1] A.C. Kak, M. Slaney, Principles of Computerized Tomographic Imaging, IEEE Press, New York, 1988.
[2] F. Peyrin, L. Garnero, I. Magnin, Trait. Signal 13 (1996) 381.
[3] A. Snigirev, I. Snigireva, V. Kohn, S. Kuznetsov, I. Schelokov, Rev. Sci. Instrum. 66 (1995) 5486.
[4] P. Cloetens, R. Barrett, J. Baruchel, J.P. Guigay, M. Schlenker, J. Phys. D: Appl. Phys. 29 (1996) 133.
[5] P. Cloetens, M. Salomé, J.Y. Buffière, G. Peix, J. Baruchel, F. Peyrin, M. Schlenker, J. Appl. Phys. 81 (1997) 5878.
[6] P. Cloetens, W. Ludwig, J. Baruchel, D. Van Dyck, J. Van Landuyt, J.P. Guigay, M. Schlenker, Appl. Phys. Lett. 75 (1999) 2912.
[7] D.M. Paganin, Coherent X-Ray Optics, Oxford Univ. Press, 2006.
[8] P. Dhez, P. Chevallier, T.B. Lucatorto, C. Tarrio, Rev. Sci. Instrum. 70 (1999) 1907.
[9] B. Golosio, et al., J. Appl. Phys. 94 (2003) 145.
[10] M. Álvarez-Murga, et al., Phys. Rev. Lett. 109 (2) (2012) 025502, http://dx.doi.org/10.1103/PhysRevLett.109.025502.
[11] A. King, et al., Science 321 (2008) 382.
[12] J. Baruchel, J. Härtwig, Encyclopaedia of Condensed Matter Physics, Elsevier, 2005, pp. 342–348.
[13] D. Lübbert, et al., J. Appl. Crystallogr. 38 (2005) 91.
[14] A. Authier, Dynamical Theory of X-Ray Diffraction, Oxford Univ. Press, 2001.
[15] A. Authier, S. Lagomarsino, B.K. Tanner (Eds.), X-Ray and Neutron Dynamical Diffraction, Theory and Applications, Plenum, New York, 1996.
[16] B.K. Tanner, D.K. Bowen (Eds.), Characterization of Crystal Growth Defects by X-Ray Methods, Plenum, New York, 1980.
[17] V.F. Petrenko, R.W. Whitworth, Physics of Ice, Oxford Univ. Press, 1999.
[18] A. Higashi, Lattice Defects in Ice Crystals, Hokkaido Univ. Press, Sapporo, Japan, 1988.
[19] R.K. Ham, Philos. Mag. 6 (11) (1961).
[20] M. Anikin, O. Chaix, E. Pernot, B. Pelisier, M. Pons, A. Pish, C. Berard, P. Grosse, C. Faure, Y. Grange, G. Basset, C. Moulin, R. Madar, Mater. Sci. Forum 338–342 (2000) 13.
[21] T. Buonassisi, et al., Appl. Phys. Lett. 89 (2006) 042102.
[22] J. Villanova, J. Segura-Ruiz, T. Lafford, G. Martinez-Criado, J. Synchrotron Rad. 19 (2012) 521.
[23] D. Shechtman, et al., Phys. Rev. Lett. 53 (1984) 1951.
[24] M. Boudard, et al., Philos. Mag. Lett. 71 (1995) 11.
[25] H. Nguyen Thi, et al., Phys. Rev. E 74 (2006) 031605.
[26] A. Buffet, et al., Phys. Stat. Sol. (a) 204 (2007) 2503.
[27] V.D. Golyshev, M.A. Gonik, V.B. Tsvetovsky, J. Cryst. Growth 237–239 (2002) 735.
[28] C. Dong, et al., J. Mater. Res. 6 (1991) 2637.
[29] J. Gastaldi, et al., Philos. Mag. 83 (2003) 1.
[30] G. Reinhart, et al., Metall. Mater. Trans. A Phys. Metall. Mater. Sci. 39 (2008) 865.
[31] J. Gastaldi, et al., Philos. Mag. 86 (2006) 335.
[32] O. Ludwig, M. Di Michiel, L. Salvo, M.M. Suéry, P. Falus, Metall. Mater. Trans. A Phys. Metall. Mater. Sci. 36 (2005) 1515.
[33] N. Limodin, et al., Acta Mater. 57 (2009) 2300.
[34] S. Terzi, et al., Acta Mater. 58 (2010) 5370.
[35] M. Suéry, S. Terzi, B. Mireux, L. Salvo, J. Adrien, E. Maire, JOM J. Miner. Met. Mater. Soc. 64 (2012) 83.
[36] D. Tolnai, P. Townsend, G. Requena, L. Salvo, J. Lendvai, H. Degischer, Acta Mater. 60 (2012) 2568.
[37] J.L. Fife, M. Rappaz, M. Pistone, T. Celcer, G. Mikuljan, M. Stampanoni, J. Synchrotron Rad. 19 (2012) 352.

[38] L. Salvo, et al., Mater. Sci. Forum 706–709 (2012) 1713.
[39] http://3dviewer.neurofly.de/.
[40] http://rsbweb.nih.gov/ij/plugins/3d-convex-hull/index.html.
[41] A. Bogno, et al., Trans. Indian Inst. Met. 62 (2009) 427.
[42] R. Mathiesen, L. Arnberg, H. Nguyen-Thi, B. Billia, JOM J. Miner. Met. Mater. Soc. 64 (2012) 76.
[43] J. Baruchel, in: G. Müller, J.-J. Métois, P. Rudolph (Eds.), Crystal Growth, from Fundamentals to Technology, Elsevier, Amsterdam, 2004, p. 345.